Manufacturing Science and Engineering Conference
MSEC 2018
June 18-22, 2018, Texas A&M University, College Station, Texas, USA

MSEC2018-6477

LAYERWISE IN-PROCESS QUALITY MONITORING IN LASER POWDER BED FUSION

Farhad Imani
Industrial and Manufacturing Engineering,
Pennsylvania State University, State College,
Pennsylvania, United States

Aniruddha Gaikwad
Mechanical and Materials Engineering Department
University of Nebraska-Lincoln
Lincoln, Nebraska, United States

Mohammad Montazeri
Mechanical and Materials Engineering Department
University of Nebraska-Lincoln
Lincoln, Nebraska, United States

Prahalada Rao
Mechanical and Materials Engineering Department
University of Nebraska-Lincoln
Lincoln, Nebraska, United States

Hui Yang
Industrial and Manufacturing Engineering,
Pennsylvania State University, State College,
Pennsylvania, United States

Edward Reutzel
Applied Research Laboratory,
Pennsylvania State University, State College,
Pennsylvania, United States

Abstract. The goal of this work is to understand the effect of process conditions on part porosity in laser powder bed fusion (LPBF) Additive Manufacturing (AM) process, and subsequently, detect the onset of process conditions that lead to porosity from in-process sensor data. In pursuit of this goal, the objectives of this work are two-fold:

(1) Quantify the count (number), size and location of pores as a function of three LPBF process parameters, namely, the hatch spacing (H), laser velocity (V), and laser power (P).

(2) Monitor and identify process conditions that are liable to cause porosity through analysis of in-process layer-by-layer optical images of the build invoking multifractal and spectral graph theoretic features.

This is important because porosity has a significant impact on the functional integrity of LPBF parts, such as fatigue life. Furthermore, linking process conditions to sensor signatures and defects is the first-step towards in-process quality assurance in LPBF. To achieve the first objective, titanium alloy (Ti-6Al-4V) test cylinders of 10 mm diameter × 25 mm height were built under differing H, V, and P settings on a commercial LPBF machine (EOS M280). The effect of these parameters on count, size and location of pores was quantified based on X-ray computed tomography (XCT) images. To achieve the second objective, layerwise optical images of the powder bed were acquired as the parts were being built. Spectral graph theoretic and multifractal features were extracted from the layer-by-layer images for each test part. Subsequently, these features were linked to the process parameters using machine learning approaches. Through these image-based features, process conditions under which the parts were built was identified with the statistical fidelity over 80% (F-score).

Keywords: Laser Powder Bed Fusion, Porosity, In-process Monitoring, Image Analysis, Spectral Graph Theory, Multifractal Analysis.

1. Introduction

Powder bed fusion (PBF) refers to a family of Additive Manufacturing (AM) processes in which thermal energy selectively fuses regions of a powder bed [1]. Figure 1 shows the schematic of the PBF process that embodies a laser power source for melting the material, accordingly, the convention is to refer to the process as Laser Powder Bed Fusion (LPBF). A galvanic mirror scans the laser across the powder bed. The laser is focused on the bed with a spot size on the order of 50 μm – 100 μm in diameter, the laser power is typically maintained in the range of 200 W to 400 W, and the linear scan speed of the laser is varied in the 200 mm/s to 2000 mm/s range [2]. In the PBF process, a layer of powder material is spread across a build plate. Certain areas of this layer of powder are then selectively melted (fused) with an energy source, such as a laser or electron beam. The bed is lowered and another layer of powder is spread over it and melted [2]. This cycle continues until the part is built.

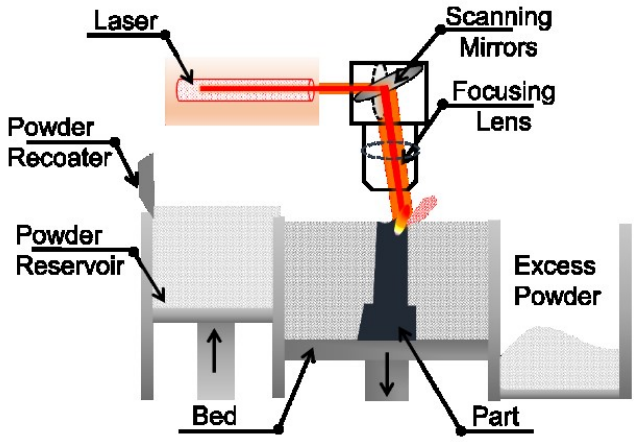

Figure 1: The schematic diagram of the laser-based powder bed fusion (LPBF) process.

1.1 Motivation

The ability of LPBF to produce intricate geometry parts from hard-to-process materials, such as cobalt-chrome and nickel-based super alloys has been conclusively demonstrated for a variety of demanding applications ranging from biomedical to aerospace [3, 4]. Process repeatability and product quality, however, remain imposing barriers towards scaling LPBF to production environments [5]. Given the layer-by-layer nature of the process, a defect in a layer will be permanently sealed in by subsequent layers. These trapped defects adversely affect part performance, such as fatigue life and strength [6, 7].

A major gap in the current research lies in the lack of correlation models between process conditions and specific defects, such as porosity via the data acquired from in-situ sensors. Addressing this gap is the first-step towards in-process quality assurance in LPBF. Therefore, there is an urgent need to: (1) understand and quantify the effect of LPBF process conditions on defects, and (2) institute in-process sensing and monitoring to capture the onset of defects. Close to 50 parameters are involved in the melting and solidification process in LPBF [8].

The following types of LPBF defects have attracted the most attention: porosity, surface finish, cracking, layer delamination, and geometric distortion. These defects are tracked to the following four root causes [9, 10]:

1) poor part design, such as inadequately supported features [11];
2) machine and environmental factors, such as poor calibration of the bed and optics;
3) inconsistencies in the input powder material, such as contamination and deviations in particle distributions; and
4) improper process parameter settings, for example, inordinately high laser power causes vaporization of the material leading to pinhole porosity, while insufficient laser power prevents powder particles from fusing together leading to large acicular pores [12]. This work specifically focuses on characterizing and detecting porosity in-situ due to the improper selection of process parameters.

1.2 Objectives

The goal of this work is to quantify the effect of process conditions on part porosity in the LPBF, and subsequently, detect the onset of process conditions that lead to porosity from in-process sensor data.

In pursuit of this goal, the objectives of this work are two-fold:

1. Quantify the effect of three LPBF process parameters, namely, laser power (P), hatch spacing (H), and velocity (V) on the size, frequency, and location of pores using X-ray computed tomography (XCT) scan data of the part.
2. Monitor and discriminate process conditions that are liable to cause porosity using in-process optical images of the powder bed invoking multifractal and spectral graph theoretic analysis.

The first objective is realized by simultaneously building nine tungsten alloy cylinders on a commercial LPBF machine (EOS M280) at varying P, H, and V conditions, and quantifying their effect on the pore spatial distribution frequency, size and location are quantified using XCT images.

The second objective is achieved by acquiring layer-by-layer optical images of the parts while they are being built, and then extracting statistical, multifractal and spectral graph theoretic features from these images. These features are subsequently used in various classification approaches such as neural networks to ascertain their ability to isolate process conditions that are liable to produce parts with severe pores.

The rest of this paper is structured as follows. A brief review of the literature is presented in Sec. 2; Sec. 3 describe the experimental conditions and layer-by-layer acquisition of part images; Sec. 4 describes the spectral graph theory and multifractal analysis of in-process image data for feature extraction and process modeling, and conclusions and avenues for future work are presented in Sec. 5.

2 Literature Review

2.1 Analysis of process parameters on defects

Beuth *et al.* have established process maps to correlate areal energy density ($E_A = \frac{P}{H \times V}$ J/mm^2) with porosity and residual stresses [13-15]. Their studies indicate that as the energy density increases beyond a threshold, the process enters the keyhole melting mode wherein the laser beam penetrates deep into the powder bed, through several layers, and causes the material to vaporize. The pores resulting from operating in the keyhole melting mode are termed as gas pores; they are typically in the region of 10 µm [9].

In contrast, when the energy density is insufficient to fuse the material, the pores formed are large and irregular, often approaching 50 µm -100 µm, and beyond range. Aboulkhair *et al.* [12, 16] and Stucker *et al.* [17-19] report process optimization studies related to porosity in LPBF with conclusions in line with findings by Beuth *et al*. While, most of the existing process maps relate the effect of energy density (E_A) to porosity with the aid of X-ray computed tomography, a

conspicuous gap is in relating pore size, density and location simultaneously with E_A. This work addresses the foregoing gap through Objective 1.

2.2 Sensing and Monitoring of defects in LPBF

Comprehensive review articles for in-process sensing are available in Ref. [9, 20-23]. Significant research in process sensing and control for metal AM processes is being done in academe and national laboratories [24-30]. Nassar and Reutzel, *et al.* experimented with imaging of the LPBF powder bed under various illumination conditions[27, 30, 31]. The resulting layer data was analyzed, and defects, such as voids caused by improper raking of the powder across the bed were identified. Lane *et al.* at NIST integrated an LPBF machine (EOS M270) with thermal and high-speed cameras, and a photodetector [24]. NIST and Edison Welding Institute (EWI) are currently building a customized LPBF testbed instrumented with multiple sensors [29, 32]. A large body of work in sensing and monitoring in LPBF is reported by the Kruth group [33-37] and Witt group [38-41] in Europe.

To detect evolving process anomalies researchers have sought to incorporate sensing techniques such as vibration, CCD video imaging, infrared and ultraviolet imaging, pyrometers, photodiodes, ultrasonic wave generators in AM machines Refs. [38, 42-46]. An early example (1994) was presented by Melwin *et al.* [47], who used a video-micrography apparatus bearing band pass and polarizing filters for observing the meltpool in polymer LPBF.

In a series of related works, Craeghs *et al.* [34-37] describe optical-based approaches for monitoring build quality in PBF by imaging the thermal behavior at the meltpool. Craeghs *et al.*, were able to detect process defects, such as deformation and overheating using their optical system [35]. Bartkowiak [48] describes a PBF apparatus integrated with a spectrometer for *in situ* measurement of the layer melt characteristics, such as emissivity. Other researchers, e.g., Chivel *et al.* [49], and Jacobsmuhlen *et al.* [38] have also developed optical imaging systems for process monitoring in AM [49]. In a recent work, Rieder *et al.* [45] used an ultrasonic sensing system for tracking build status in PBF. A broadband ultrasonic sensor mounted on the underside of the build plated is used to detect voids, akin to acoustic microscopy

Craeghs *et. al* [35, 50, 51] report that the amplitude of the photodiode signal is correlated with the melt-pool area and the melt-pool temperature. They subsequently use this information to identify process failures, such as detection of deformation due to thermal stresses and overheating at overhang structures, in each build layer. Further, they developed a feedback control sensor based on optical images. Chivel and Smurov [49] use two different wavelengths and selected temperature profiles to extract information of the bed temperature distribution, and the size of the meltpool for process monitoring.

A main drawback in most of these studies is that they do not connect practical process conditions to defects, but rather focus on artificially inducing flaws by way of catastrophic process anomalies. Furthermore, the analytical techniques rely on classical time-series signal processing techniques, which may not be effective in capturing subtle defects. Recent progress to overcome this limitation is reported by the Clare group at Nottingham University who have used spatially resolved acoustic spectroscopy (SRAS) to detect porosity in-situ in LPBF, wherein the amplitude of a surface acoustic wave generated by laser is correlated with the location and severity of porosity at different laser power settings [52, 53]. The current work addresses this extant gap through Objective 2.

3 Experimental Setup and Data Acquisition

Experiments were conducted on an EOS M280 LPBF machine. The input material was a Titanium alloy, ASTM B348 Grade 23 Ti-6Al-4V powder material whose particle size ranges from 14 µm to 45 µm. The parts analyzed in this study are cylinders which were printed by varying the hatch spacing (H), scan velocity (V) and laser power (P). The cylinders are 25 mm in length and 20 mm in diameter.

Table 1 shows the seven process parameter settings which were used to print these cylinders. The nominal settings are labeled as H0 = 0.12 mm, V0 = 1250 mm/s, and P0 = 340 W. Hatch spacing and laser print velocity are increased by 25% and 50%, and laser powder has been decreased by 25% and 50% from their nominal settings. The three process settings are aggregated in terms of the areal energy density applied for melting called the Andrew number: $E_A = \frac{P}{H \times V}$ J/mm^2.

A digital single-lens reflex camera (DSLR, Nikon D800E) along with multiple flash-lamps placed inside the build chamber are used to capture the layer-by-layer powder bed images. Images are captured at two instances in every layer, namely, post laser scan and post re-coat. The camera shutter is controlled by a proximity sensor that registers the location of the re-coater blade. Five images of the powder bed images are captured under bright-field and dark-field flash settings. The layout of the camera and flash-lamp location are shown in Figure 2, and the representative images under the five light schemes are shown in Figure 3. In this work, images from bright-field light scheme in Figure 3(a) are analyzed. Details of the experimental setup are available in Ref. [31].

Table 1: The combination of power (P), hatch spacing (H), scan velocity (V) process conditions used for making the titanium alloy parts.

Process Condition (P, H, V) [W, mm, mm/sec]		E_A [J.mm^{-2}] Andrew's number
P0, H0, V0	(340, 0.12, 1250)	2.27
P -25%, H0, V0	(255, 0.12, 1250)	1.70
P-50%, H0, V0	(170, 0.12, 1250)	1.13
P0, H +25%, V0	(170, 0.15, 1250)	1.81
P0, H +50%, V0	(170, 0.18, 1250)	1.51
P0, H0, V +25%	(170, 0.12, 1562)	1.81
P0, H0, V +50%	(170, 0.12, 1875)	1.51

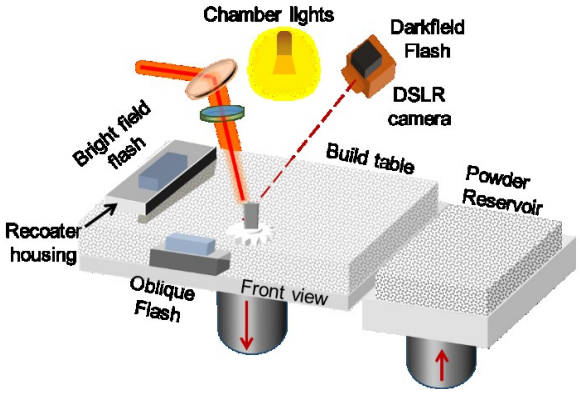

Figure 2: Schematic diagram of the location of flash-lamps and camera used to capture in-situ powder bed images [31].

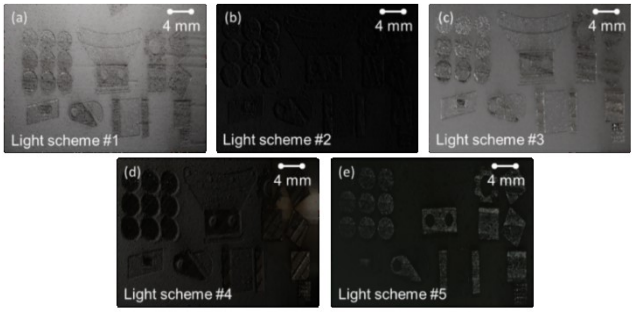

Figure 3: Cropped image of the powder bed in different light schemes.

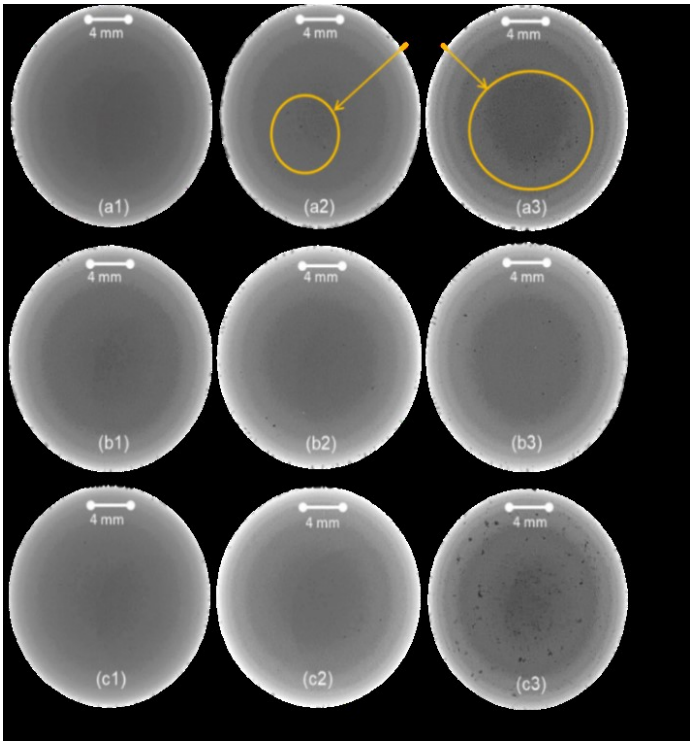

Figure 4: Effect of process conditions on the parts as seen in XCT scan images. Pore frequency increases as process conditions drift from nominal conditions. Highest number of pores are seen in the part printed at P -50 % (c3)

4 Methodology and Results

The LPBF process data is analyzed in two phases, namely, (1) offline analysis of X-ray computed tomography (XCT) data in Sec. 4.1; and (2) analysis of in-situ images of the powder bed in Sec. 4.2.

4.1 Phase 1: Offline analysis of porosity.

This section aims to analyze the effect of hatch spacing (H), laser velocity (V), and laser power (P) on the count, size, and location of pores. Representative XCT images of parts under different P, H and V conditions are shown in Figure 4.

A visual inspection of the XCT scans shows that the size and number (count) of the pore is inversely proportional to the energy density (E_A). The following inference are made based on Figure 4.

- The severity of pores is influenced by all three process parameters. However, laser power (P) seems to have an inordinately high effect.
- As Andrew's number (E_A) is reduced, the size and number of the pores become larger.

These observations are quantified by extracting count, size and location attributes by analyzing the XCT scan images through the steps shown in Figure 5.

- Figure 5 (a) - XCT scans for 30 randomly chosen cross-sectional areas are analyzed.
- Figure 5 (b) and (c) - The XCT scan images are binarized based on a heuristically determined threshold. Some information is inevitably compromised during the binarization process. A complement of the binary image is taken to return a black background, which makes computation easier as the image matrix becomes sparse.
- Figure 5 (d) - To reduce noise induced due to binarization a nearest neighborhood approach is used [54]. We note that while it is customary to refer to voxels in the context of XCT, because the images are converted to binary images (binarized), we revert to using the term pixel. In this procedure, a binarized XCT pixel is labeled as a defect only if it is connected to the 8-nearest pixels. In other words, if the 8 nearest neighboring pixels of a particular pixel are also bright (i.e., 1), then the pixel is deemed to represent part of a defect.

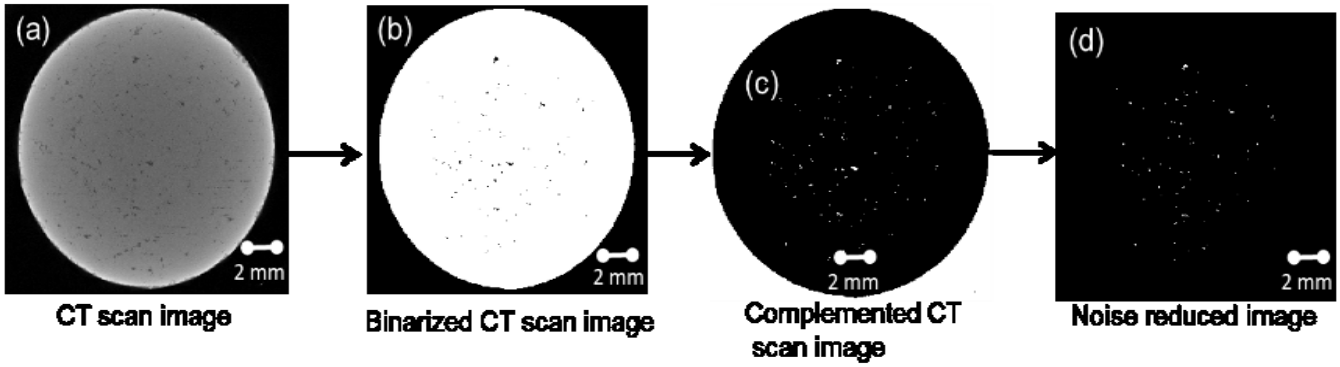

Figure 5: An overview of the image processing methodology used to analyze the computed tomography (XCT) scan images. (a) XCT scan image of part printed with P -50 %, (b) binarization of the XCT scan image of the part, (c) complemented binary image of the XCT scan image, and (d) noise reduced XCT scan image which is used for the spatial distribution analysis

Next, the pore count, size and location are extracted as follows:

- Pore count – The number of 8-connected binarized XCT pixel over a layer translates to the pore count.
- Size of pores – The size of a pore is grouped into one of 5 classes contingent on its radius. Each pore is considered as an annular structure on the noise reduced image, and then, the number of pixels within each annulus is calculated. Depending on the number of pixels in the annulus, the pores are classified into various radii, namely 1-5 pixel radii. A radius of one-pixel unit equates to a pore radius of 16 μm on the part.
- Pore Location – The pore location is determined by segmenting the XCT scan image into 5 concentric areas as shown in Figure 6. The number of pores in each 1-mm thick segment of the XCT scan image is then counted. This establishes the distance of the pores from the center of the cylinder.

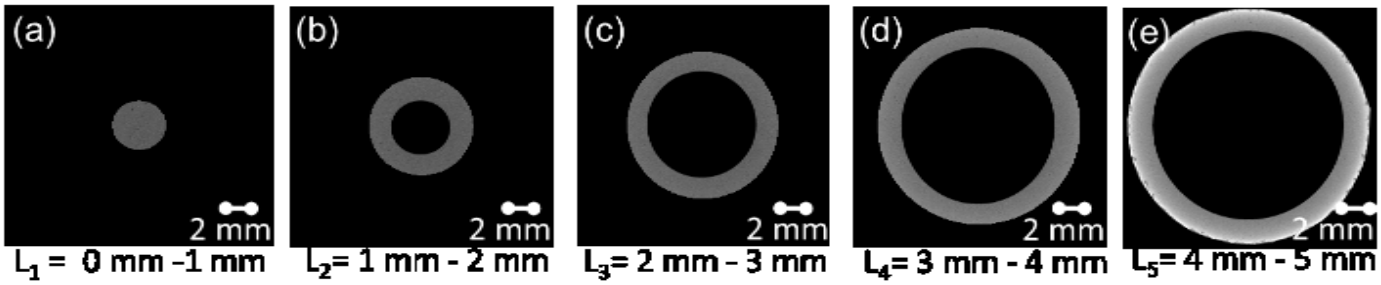

Figure 6: An example of the procedure followed to divide XCT scan image of a part into concentric segments. (a) First segment 0 mm – 4 mm of the XCT scan image (L_1), i.e., the segment that encompasses the center of the XCT scan image, (b) second segment 4 mm – 8mm of the XCT scan image (L_2), (c) third segment 8 mm – 12 mm of the XCT scan image (L_3), (d) fourth segment 12 mm – 16 mm of the XCT scan image (L_4), and (e) last segment 12 mm – 16 mm of the XCT scan image (L_5), i.e., the segment which is farthest from the center of the XCT scan image.

a) Effect of process parameters on count and size of pores

Analysis of the XCT scan images shows that decrease in the areal energy density (EA) leads to an increase in the count (number of pores) and size of pores. This effect of laser power (P), hatch spacing (H), and laser print velocity (V) on pore count and size is exemplified in Figure 8 from which the following inferences are drawn. In Figure 8, the x-axis is the pore size, and the y-axis is the mean count (or number) of the pore observed on 30 randomly selected slices of the XCT scan. These results are also detailed in Table 2, which reports the mean number of pores, rounded to the nearest integer, along with the standard deviation for 30 randomly chosen layers.

- Referring to Figure 8 (a), the pore distribution in terms of count vs. pore size is plotted for different levels of laser power (P). The decrease in laser power by 50% (170 W) leads to almost a 100-fold increase in the number of pores. Further, parts produced under P -50% (170 W) have pores ranging from 1 pixel to 4 pixels in size, i.e., 28 μm to 112 μm, whereas parts produced under nominal power (P0= 340 W) and P -25% (270 W) have pores of radius 2 pixels (~ 32 μm) at most.
- Referring to Figure 8 (b), increasing the hatch spacing (H) leads to an increase in both the count and size of pores. The

magnitude of the effect of laser hatch spacing is significantly smaller than that of laser power. In case of varying hatch spacing (Figure 8 (b)), the highest number of pores are seen in the cylinder which is printed with H +50 %, i.e., 0.18 mm hatch spacing. From Figure 8 (b), for all the three levels of hatch spacing, the largest pore radius observed is 2 pixels.

- Referring to Figure 8 (c), akin to hatch spacing, increase in laser print velocity (V) leads to increase in count and size of pores. The largest pore size of radius 3 pixels (~48 µm) was recorded in the cylinder printed with V +50 % (1875 mm/s). The effect of velocity on porosity is least consequential of the three factors studied in this work.

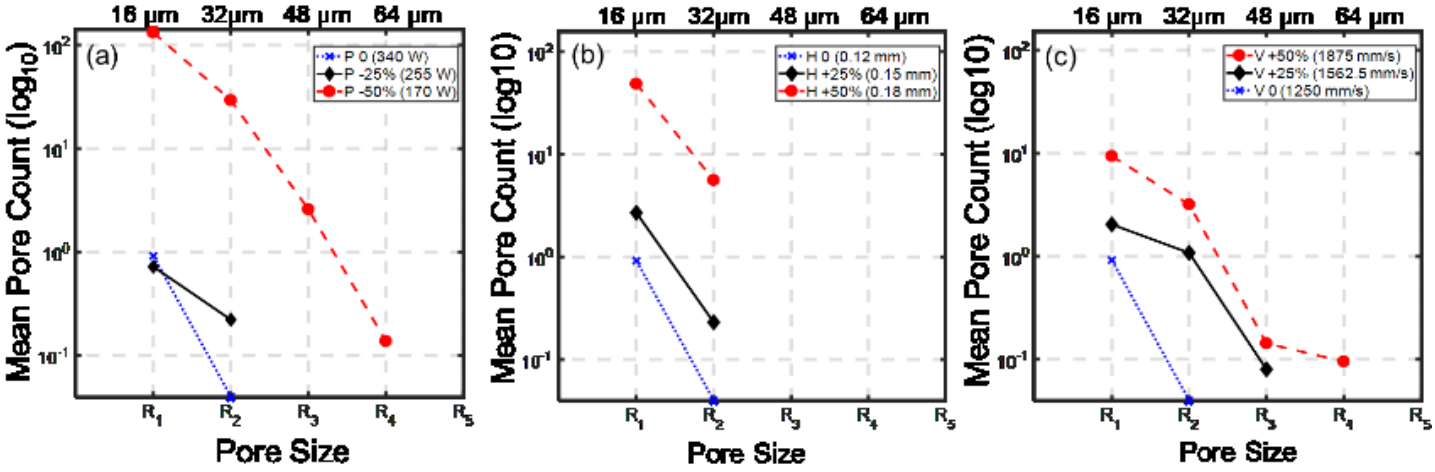

Figure 7: Count of pores vs. Pore size in varying process conditions. (a) In P -50 % printing condition highest number of pores are seen of size R1 (16 µm), and in P0 and P -25 % printing condition, very few pores of size R1 (16 µm) are seen. (b) In parts printed with varying hatch spacing only pores of size R1 (16 µm) and R2 (32 µm) are seen, and the highest number of pores is seen in H +50 % printing condition. (c) In comparison with other printing conditions, the lowest number of pores is seen in parts printed with varying velocity. Pores of size R1 (16 µm) are highest in number in V0, V +25 %, and V +50 % printing conditions.

b) Effect of process parameters on the location of pores

The location of pores in the test cylinders is determined by segmenting the XCT scan image of a cylinder into 5 concentric parts as described previously in the context of Figure 6. This establishes the distance of the pores from the center of the cylinder. The mean and standard deviation of pores in each segment of the part for 30 randomly chosen layers are reported in in Figure 8, from which the following inferences are drawn:

- Referring to Figure 8 (a), it is evident that as the laser power decreases, more number of pores are recorded in the L_2 (4 mm – 8 mm) to L_4 (8 mm – 12 mm) segment, of the cylinder. Figure 8 (a) further reveals that the cylinder printed with nominal laser power (340 W) has most number of pores in the first two annular segments of length L_1 (0 mm – 4 mm) and L_2 (4 mm – 8 mm), which indicates that the pores are located close to the center. This trend is also observed in the cylinder printed with P -25 % laser power (270 W). In contrast, the cylinder printed with -50 % laser power has most number of pores in the third segment 8-12 mm.

- Referring to Figure 8 (b) and (c), in cylinders printed with varying hatch spacing (H) and laser print velocity (V), respectively it is observed that parts produced at +50% hatch spacing (0.18 mm) and laser print velocity (1875 mm/s) have the highest number of pores at the radial distance with L_3 (8-12 mm). Pores in the cylinders printed with +25% and nominal hatch spacing and laser print velocity are mainly located in the first two segments 0 mm - 1 mm and 1 mm - 2 mm.

The sharp drop in porosity in L_5 is likely due to the reason that the external boundary of the part is scanned with increased E_A after the rest of the part (post-contour melting). The added heat at the periphery mitigates porosity in L_5. Further, the concentration of heat in the core of the part may explain the reduced porosity towards the center (L_1). Lastly, the effect of thresholding to convert may lead to a loss of information, this last reason can be largely discounted in the light of Figure 5(a and d), wherein pores in the boundaries are captured appreciably.

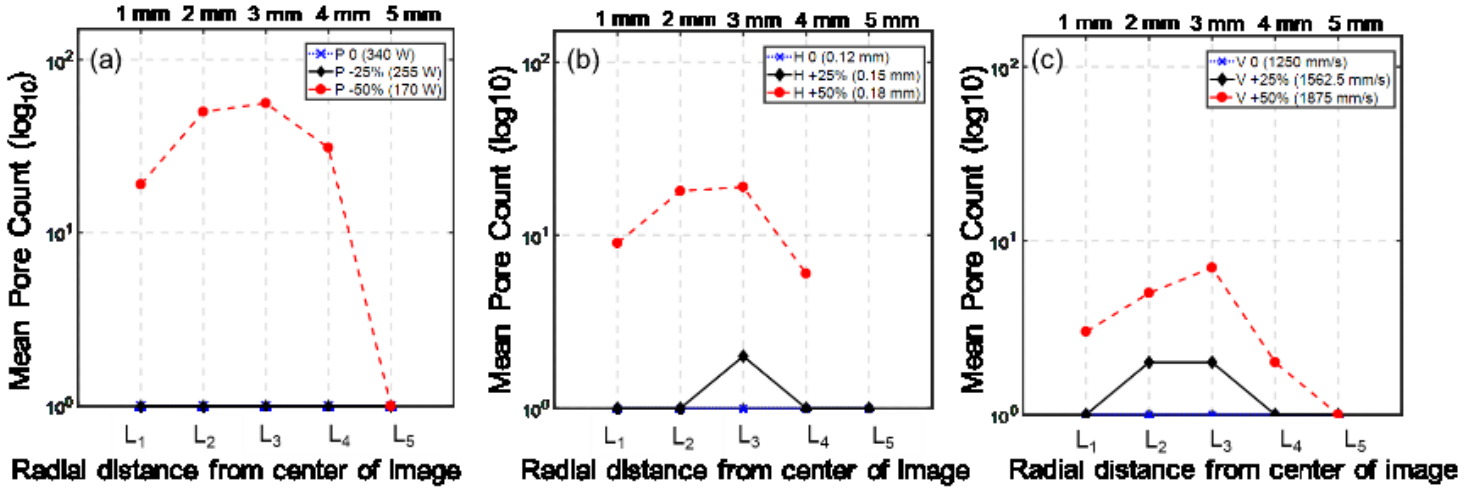

Figure 8: Mean pore count vs. radius from center of image at varying process conditions. (a) Parts printed with laser power of P -50 % have highest number of pores in the third segment (L3= 2-3mm) of the XCT scan image. Parts printed with P 0 (nominal condition), and P -25 % have pores located in second segment (L2= 1-2 mm) of the XCT scan image. (b) In parts printed with varying hatch spacing highest number of pores are seen in the third segment (L3= 2-3 mm) of the XCT scan image in all conditions. (c) In parts printed with varying velocity highest number of pores are seen in V +50 % in the third segment (L3= 2-3 mm), and in V0 and V +25 % conditions, highest number of pores are seen in the second segment (L2= 1-2 mm) of the XCT scan images.

4.2 Phase 2: Analysis of online data of laser powder bed fusion process (LPBF).

This section links the process conditions to the layer-by-layer images of the parts as they are melted. This will allow detection of process drifts in their early stages. For this purpose, two methods are proposed, the first based on spectral graph theory, and the second on multifractal and lacunarity analysis.

a) Application of spectral graph theory for image analysis

Spectral graph theoretic Laplacian eigenvalues extracted from online images are used to identify the process conditions under which a part is produced. The approach has the following two steps.

Step 1: Representing the image of each part as a graph.

A layer-wise image obtained from the DSLR camera for a laser sintered cylinder layer with M × N pixels can be represented by a matrix $\boldsymbol{X}^{M\times N}$. As shown in Figure 9, each row of the matrix X is considered as a row vector and it represents a node or vertex (V) of an undirected graph which is denoted as $G \equiv (V, E)$, where E is the edges in the graph [55]. The M row vectors of the matrix X are represented as $\boldsymbol{a}_K, K = \{1,2,\dots \mathrm{M}\}$.

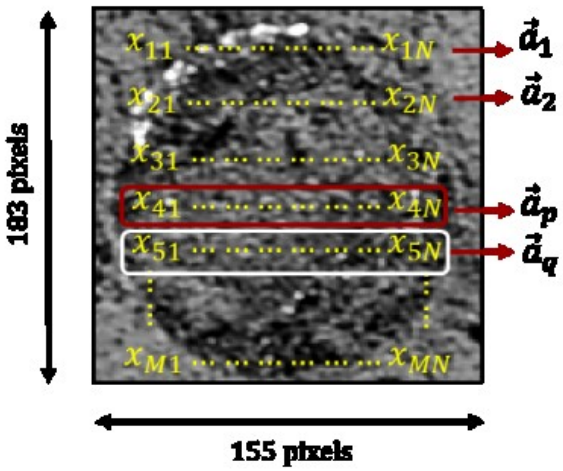

Figure 9: An in-situ image of part depicting the row vectors which are used for pairwise comparison.

Further, a pairwise comparison is performed between each of the row vectors through a kernel function Ω [56]. A pairwise comparison along the columns has been shown to lead to similar results as long as the image is homogeneous [57].

$$w_{pq} = \Omega(\overrightarrow{a_p}, \overrightarrow{a_q}) \; \forall \; p, q \in K \qquad (1)$$

The kernel function Ω used in this study to compute the pairwise comparison is the radial basis kernel function (Eqn. (2) and (3)) .

$$w_{pq} = e^{-\left[\frac{E}{\sigma_X}\right]^2} \qquad (2)$$

$$\boldsymbol{E} = \left[\left\|\overrightarrow{\boldsymbol{a}_p} - \overrightarrow{\boldsymbol{a}_q}\right\|^2\right] \qquad (3)$$

where, σ_X is the overall standard deviation of E. Next, a binary similarity matrix $\boldsymbol{S} = [w_{pq}]$ is created with help of a threshold function. This threshold function θ when applied to w_{pq} converts it into binary form[58].

$$\Theta(w_{pq}) = \mathrm{w}_{pq} = (0,1) \qquad (4)$$

This threshold function facilitates in determining whether there is a connection between two nodes [58]. w_{pq}= 1 if there is a connection and otherwise it is zero.

$$\Theta(w_{pq}) = \mathrm{w}_{pq} = \begin{cases} 1, w_{pq} \le r \\ 0, w_{pq} > r \end{cases} \qquad (5)$$

Here r is given by,

$$r = \frac{\sum_{p=1}^{p=\mathrm{M}} \sum_{q=1}^{q=\mathrm{M}} \mathrm{w}_{pq}}{\mathrm{M}^2} \qquad (6)$$

Step 2: Extracting features from the graph.

Once a graph is formulated from the image, topological features are extracted from the graph. These features are useful in classification of parts which are made with different process parameters. The first step towards feature extraction is computing the degree d_p of a node p, i.e., the number of edges that pass through the node p. The degree of node p is computed by summing each row in the similarity matrix $\boldsymbol{S}$. From the degree of node d_p, a diagonal degree matrix $\boldsymbol{\mathcal{D}}$ is formed as follows,

$$\boldsymbol{\mathcal{D}} \stackrel{\text{def}}{=} \mathrm{diag}(d_1, \cdots, d_M) \qquad (7)$$

Now, with the help of the degree $\boldsymbol{\mathcal{D}}$ matrix and the similarity matrix $\boldsymbol{S}$, the normalized Laplacian $\boldsymbol{\mathcal{L}}$ of the graph is defined as follows,

$$\boldsymbol{\mathcal{L}} \stackrel{\text{def}}{=} \boldsymbol{\mathcal{D}}^{-\frac{1}{2}} \times (\boldsymbol{\mathcal{D}} - \boldsymbol{S}) \times \boldsymbol{\mathcal{D}}^{-\frac{1}{2}} \qquad (8)$$

where, $\boldsymbol{\mathcal{D}}^{-\frac{1}{2}} = \mathrm{diag}\left(1/\sqrt{d_1}, \cdots, 1/\sqrt{d_M}\right)$.

Finally, the Eigen spectra of the Laplacian is computed as follows [59].

$$\boldsymbol{\mathcal{L}}\boldsymbol{v} = \lambda^* \boldsymbol{v}. \qquad (9)$$

The eigenvalues (λ) of the Laplacian are used in the classification of LPBF parts per their processing conditions. In this work, the first five smallest non-zero eigenvalues are used. Also, the Kirchhoff index for each graph is computed as follows, where λ_i are the non-zero eigen values of the Laplacian.

$$K_f = 2 \times \varepsilon \times \sum_{i=2}^{\mathrm{M}} \lambda_i^{-1} \qquad (10)$$

where $\varepsilon = \frac{\sum_{i=1}^{i=\mathrm{M}} \sum_{j=1}^{j=\mathrm{M}} s_{ij}}{2}$.

The non-irradiated part of the part image i.e. the un-sintered powder, is fairly homogenous, so when it the image undergoes a row-wise comparison, the distance kernel function becomes zero. The nodes which are far apart from each other are connected on the graph.

b) Multifractal and lacunarity analysis of part images

The fractal dimension has been extensively used to characterize the texture and patterns of manufactured surfaces [60].This work goes beyond the traditional methods that extract a single fractal dimension from the surface image, but rather assume the irregularity and non-homogeneity of image data are due to the presence of several fractal dimensions [61]. As such, we extract a spectrum of multifractal features to characterize the layer-by-layer images obtained in LPBF. A fractal is defined as a shape that embodies geometric similarity across multiple scales [62]. Assuming that a fractal object occupies a limited area in the Euclidean space, then the object can be covered by *N* measure elements with size ε as follows,

$$N(\varepsilon) = \varepsilon^{-D} \qquad (11)$$

where *D* is the fractal dimension. The box-counting method is widely used to estimate the fractal dimension of an irregular object. This method covers a fractal set with measure elements (e.g., box) at different sizes and observe how the number of boxes varies with its size [63]. This procedure is repeated using different boxes of size *l*. Once the *l* becomes sufficiently small, *N(l)* being the number of boxes that are needed to cover a fractal object with the size *l*, then the box-counting dimension D_0 is defined as,

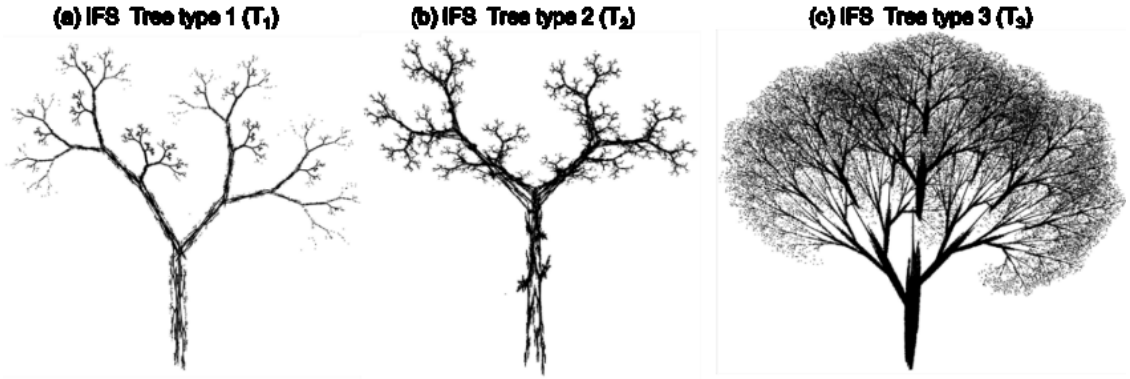

Figure 10. Simulated trees by the multifractal iterated function system, (a) IFS tree T1, (b) IFS tree T2, (c), IFS tree T3. All three IFS trees have the same box-counting fractal dimension of 2.0449, but different multifractal spectra as shown in Figure 11.

For example, Figure 10 shows three types of fractal objects called *multifractal trees* that are constructed with the iterated function systems (IFS) method. These fractal trees are labeled T_1, T_2, and T_3. The estimates of fractal dimension (D_0) using the box-counting method in Figure 10 are $D_0 = 2.0449$ for all three fractal trees. However, three trees show high levels of self-similarity, irrgularity and heterogeneity due to the presence of a spectrum of fractal dimensions. This demonstrates that the traditional box-counting fractal dimension is limited in the ability to fully characterize the patterns of multifractal objects [64]. Multifractal analysis provides a means to overcome this limitation of traditional fractal dimensions. The procedure to estimate the multifractal spectrum from image data is as follows,

Step 1: Estimating the local densities function ($P_i(L)$).

$$P_i(L) = \frac{N_i(l)}{N_T} \tag{12}$$

where $N_i(l)$ is the number of mass or pixels in the i^{th} box of size l, N_T is the total mass of a set and $P_i(l)$ is the probability in the i^{th} box.

Step 2: Calculating singularity strength exponent (l^{α_i}).

$$P_i(l) \sim l^{\alpha_i} \tag{13}$$

where α_i reflects the local behavior of $P_i(l)$ in the i^{th} box with size l and it can be derived as

$$\alpha_i = \lim_{l \to 0} \frac{\ln P_i(l)}{\ln l} \tag{14}$$

Step 3: Estimating multifractal spectrum ($f(\alpha)$).

The multifractal spectrum $f(\alpha)$ is the fractal dimension of the set of locations that have same values for singularity strength exponents α_i. Given the number of boxes $N(\alpha)$ where the probability $P_i(l)$ has exponent values between α and $\alpha + d\alpha$ the multifractal spectrum $f(\alpha)$ can be calculated as follows,

$$D_0 = \lim_{l \to 0} \frac{\ln N(l)}{\ln\left(\frac{1}{l}\right)}$$

$$f(\alpha) = \lim_{l \to 0} \frac{\ln N(\alpha)}{\ln(1/l)} \tag{15}$$

Step 4: Characterizing multifractal measures (D_q).

Multifractal measures are characterized by the scaling of the q^{th} moments of $P_i(l)$ distributions as,

$$\sum_{i=1}^{N(l)} P_i^q(l) = l^{\tau(q)} \tag{16}$$

where $\tau(q)$ is called the mass exponent of q^{th} order moment. Then, the generalized fractal dimensions D_q is written as,

$$D_q = \frac{\tau(q)}{q-1} \tag{17}$$

Then, the Legendre transformation is used to derive the multifractal spectrum as,

$$f(\alpha(q)) = q\alpha(q) - \tau(q) \tag{18}$$

$$\alpha(q) = \frac{d\tau(q)}{dq} \tag{19}$$

However, Legendre transformations is computationally demanding in the calculation of $f(\alpha)$. Also, this approach requires smoothing the D_q curve which causes errors in the estimated $f(\alpha)$ [65]. To overcome this limitation and bypass intermediate smoothing steps in estimating $f(\alpha)$, a family of normalized measures $\mu_i(q,l)$ as q^{th} moments of mass probability $P_i(l)$ are introduced in Eqn.(20). A constant l range is also used to avoid multifractal properties over a small interval of scales.

$$\mu_i(q,l) = \frac{P_i^q(l)}{\sum_{i=1}^{N(l)} P_i^q(l)} \tag{20}$$

As such, the multifractal spectrum $f(\alpha)$ and the average singularity strength exponent $\alpha(q)$ can be written as,

$$f(\alpha(q)) = \lim_{l \to 0} \frac{\sum_{i=1}^{N(l)} \mu_i(q,l) \ln[\mu_i(q,l)]}{\ln l} \tag{21}$$

$$\alpha(q) = \lim_{l \to 0} \frac{\sum_{i=1}^{N(l)} \mu_i(q,l) \ln[P_i^q(l)]}{\ln l} \tag{22}$$

Figure 11 shows the multifractal spectra for three IFS trees in Figure 10. It is evident that multifractal features effectively distinguish the differences in the three IFS trees that were not captured using the traditional fractal dimension. Note that the tail of the third IFS tree T3 is longer than other two IFS trees. Because T3 has more pixels with lower values (value towards 0 or black pixels) in comparison to the other two trees, and the $f(\alpha(q))$ spectrum intensifies the effect of pixels with lower values.

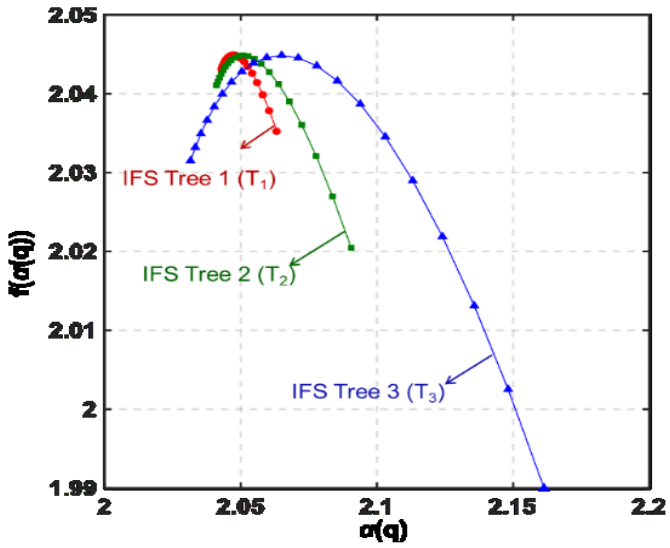

Figure 11. Multifractal spectra of IFS trees shows the self-similarity, irregularity, and non-homogeneity of fractal objects that cannot be adequately characterized using a single fractal dimension.

Futhermore, lacunarity complements multifractal analysis by characterizing the manner or distribution in which the fractal objects fills the space [66]. Lacunarity and multifractal analysis jointly describe the irregularity and non-homogeneity in fractal objects as well as how they fill the space that cannot be otherwise achived by traditional box-counting dimension or statistical features.

To obtain the lacunarity measure, a unit box of size l is placed over the object and the number of set points s (black pixels) in the image is counted – this is called the *box mass*. Next, the box is translated one space along the set, and the box mass is again determined. This process is repeated over the entire set, creating a frequency distribution of the box masses represented as $N(s,l)$. This frequency distribution is converted into a probability distribution $Q(s,l)$ by dividing by the total number of boxes $N(l)$ of a given size l [67].

$$Q(s,l) = \frac{N(s,l)}{N(l)} \tag{23}$$

The first and second moments of this distribution can be written respectively as:

$$Z_1 = \sum sQ(s,l) \tag{24}$$

$$Z_2 = \sum s^2 Q(s,l) \tag{25}$$

The lacunarity method with box size l can be computed as:

$$\Lambda(l) = \frac{Z_2}{(Z_1)^2} \tag{26}$$

In Eqn. (23), Λ(l) represents the lacunarity for the box size l. This procedure is repeated for different box sizes, and a log-log plot of the lacunarity versus the size of the box is traced. Figure 12 shows T3 has higher lacunarity values in comparison to the two other trees. The distribution of gap sizes is termed as lacunarity.

Figure 13 shows the singularity strength exponent $\alpha(q)$ and multifractal spectrum $f(\alpha(q))$ estimated from 3132 layerwise images in the LPBF process. There are 1044 images in E_A=2.27; 696 in E_A=1.81; 348 in E_A=1.70; 696 in E_A=1.51; and 348 in E_A=1.13. Note that multifractal spectra of these images show significant variations with respect to the different Andrew's numbers.

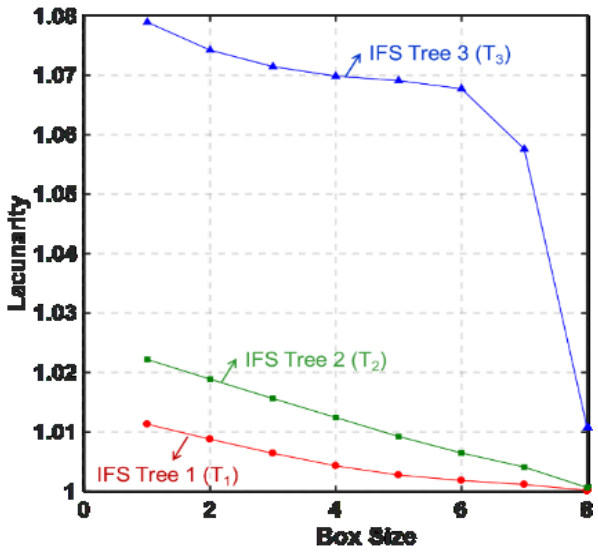

Figure 12. Lacunarity analysis of IFS trees describes how fractal objects fill the space that cannot be adequately captured using traditional fractal analysis.

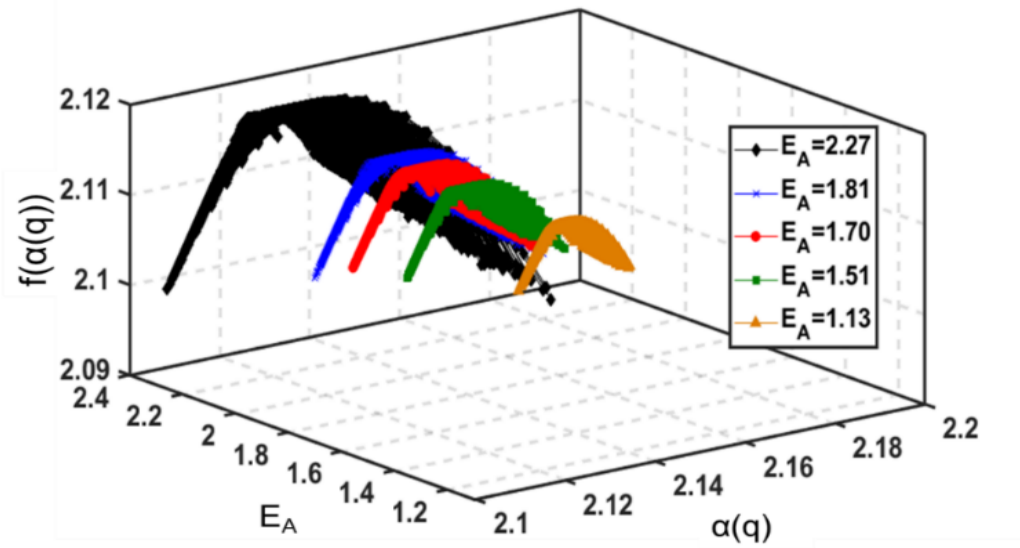

Figure 13: The varaitions of multifractal spectra w. r. t. the Andrew's Number for 3132 layerwise images in LPBF.

4.3 Application of Multifractal and Spectral Graph Theory to Online Images

Further, the parts built under the different E_A conditions described in Table 1 were classified using different machine learning approaches with various types of input features. A 70%-15%-15% split for training, testing, and validation data was imposed. The classification fidelity is reported in terms of the F-score, which is an aggregate of the Type I and Type II statistical errors. The results are summarized in Table 2.

Table 2: Accuracy of classifiers used for classification of parts using statistical, spectral graph theoretic, multifractal and lacunarity features. The numbers in parenthesis are the standard deviations from a 5-fold replication study.

Classifier	Statistical features	(A) Spectral graph theoretic features	(B) Multifractal and lacunarity features	Combined features A+B
Support Vector Machine	55.58% (0.58)	71.94% (0.20)	76.16% (0.30)	89.36% (0.21)
Complex Tree	54.10% (0.14)	68.02% (0.66)	68.60% (0.50)	79.98% (0.23)
Linear Discriminant Analysis	52.72% (0.34)	63.22% (0.49)	63.02% (0.08)	82.16% (0.21)
K-Nearest Neighbor	56.62% (0.50)	67.66% (0.25)	70.38% (0.27)	78.60% (0.34)
Ensemble (Bagged Trees)	51.06% (0.58)	72.50% (0.10)	72.64% (0.61)	85.86% (0.30)
Feed Forward Neural Network	49.66% (1.99)	64.62% (1.7)	66.54% (1.76)	84.40% (1.67)

Three types of input features are used: (1) statistical image features, namely, intensity (mean) of an image, and local standard deviation of an image in 3 × 3 neighborhood, (2) spectral graph theoretic features, namely, the first five non-zero Eigenvalues and the Kirchhoff index, and (3) the multifractal and lacunarity features. It is observed that irrespective of the classification approaches used, the spectral graph, and multifractal and lacunarity features outperform the conventional statistical features. Furthermore, combining the spectral graph and multifractal features results in F-score around 80%. The results reported in Table 2 show that the spectral graph theoretic and multifractal features discriminate the part quality with higher fidelity than traditional statistical analysis. This is valuable from the in-process quality monitoring viewpoint. In a practical scenario, images of the parts can be used to conclude whether the process within an optimal window.

5 Conclusions and Future Work

This paper presents the modeling and analysis of in-process layerwise images in LPBF to investigate the effect of LPBF process conditions on the severity, size, and location of porosity, and further connects the process conditions to sensor signatures. This is an indirect way to monitor the LPBF process. The specific outcomes of the work are as follows:

1. Three process parameters, namely, laser power (P), hatch spacing (H), and scan velocity (V) were varied during the LPBF of Ti-6Al-4V powder material. The effect of varying these parameters on porosity were characterized offline using X-ray computed tomography (XCT). Based on analysis of the XCT images the following inference is tendered. Decreasing the laser power by 50% from 340 W to 170 W leads to almost a three-fold increase in the average number of pores, compared to an equivalent percentage increase in hatch spacing, and ten-fold increase compared to scan velocity. Hence, the control of laser power is most consequential for avoiding porosity.
2. Online visible spectrum images of the part were acquired as they are built using a still camera. These images were analyzed using multifractal and graph theoretic approaches. The features extracted by applying these approaches were subsequently used within various machine learning techniques. The aim was to distinguish the process conditions under which the parts were built given an image of the part. It is observed that combining multifractal and graph theoretic analysis leads to as much as 30% increase in the accuracy of discriminating process conditions compared to using traditional statistical measurements. Using this approach, the process conditions can be isolated with F-score approaching 80%. From a practical perspective, although the P, H, and V settings are predetermined for each material in terms of the Andrew number (EA), the laser power, particularly, is liable to drift due to occlusion of the focusing optics; the vaporized material tends to condense on the lens especially during long builds.

One limitation of this work is that it does not relate the sensor signatures directly to the defects, but rather isolates the process condition that leads to porosity. This is mainly due to the fact that the resolution of the camera is not sufficient to identify pores, which are in the 16 μm – 65 μm, from the images directly. To overcome this drawback, data from multiple sensors will be combined (e.g., thermography and meltpool monitoring) to not only capture multiple types of defects simultaneously, but also improve upon the detection fidelity. Furthermore, in the future work, the authors will endeavor to understand the effect of process parameters on other type of defects, such as distortion and geometric inaccuracy.

Acknowledgements

The authors acknowledge the help provided by Mr. Cheng-Bang Chen (Penn State), Mr. Ben Bevans (UNL), and Ms. Emily Curtis (UNL). This work is supported in part by the NSF Center for e-Design (Lockheed Martin) at Penn State, and NSF grants (CMMI-1646660, CMMI-1617148, CMMI-1719388, and CMMI- 1752069 (CAREER)). The author (HY) also thank Harold and Inge Marcus Career Professorship for additional financial support. We gratefully acknowledge the valuable contributions of the faculty, staff, and students at Penn State's Center for Innovative Materials Processing through Direct Digital Deposition (CIMP-3D) for providing the data utilized in this research.

References

[1] *ASTM 52900-15 Standard Terminology for Additive Manufacturing*, 2015.

[2] I. Gibson, D. W. Rosen, and B. Stucker, *Additive manufacturing technologies: rapid prototyping to direct digital manufacturing*. Springer, 2010.

[3] N. Guo and M. C. Leu, "Additive manufacturing: technology, applications and research needs," *Frontiers of Mechanical Engineering,* vol. 8, no. 3, pp. 215-243, 2013// 2013.

[4] M. Schmidt *et al.*, "Laser based additive manufacturing in industry and academia," *CIRP Annals - Manufacturing Technology* 2017 (In-press).

[5] S. K. Everton, M. Hirsch, P. Stravroulakis, R. K. Leach, and A. T. Clare, "Review of in-situ process monitoring and in-situ metrology for metal additive manufacturing," *Materials and Design,* vol. 95, pp. 431-445, 2016.

[6] M. Gorelik, "Additive manufacturing in the context of structural integrity," *International Journal of Fatigue,* vol. 94, no. 2, pp. 168-177, 1// 2017.

[7] M. Seifi *et al.*, "Progress Towards Metal Additive Manufacturing Standardization to Support Qualification and Certification," *JOM,* journal article vol. 69, no. 3, pp. 439-455, 2017.

[8] P. O'Regan, P. Prickett, R. Setchi, G. Hankins, and N. Jones, "Metal Based Additive Layer Manufacturing: Variations, Correlations and Process Control," *Procedia Computer Science,* vol. 96, pp. 216-224, 2016.

[9] M. Grasso and B. M. Colosimo, "Process defects and in situ monitoring methods in metal powder bed fusion: a review," *Measurement Science and Technology,* vol. 28, no. 4, p. 044005, 2017.

[10] W. J. Sames, F. List, S. Pannala, R. R. Dehoff, and S. S. Babu, "The metallurgy and processing science of metal additive manufacturing," *International Materials Reviews,* vol. 61, no. 5, pp. 315-360, 2016.

[11] B. Cheng and K. Chou, "Geometric consideration of support structures in part overhang fabrications by electron beam additive manufacturing," *Computer-Aided Design,* vol. 69, pp. 102-111, 12// 2015.

[12] N. T. Aboulkhair, N. M. Everitt, I. Ashcroft, and C. Tuck, "Reducing porosity in AlSi10Mg parts processed by selective laser melting," *Additive Manufacturing,* vol. 1, pp. 77-86, 2014.

[13] J. Beuth *et al.*, "Process mapping for qualification across multiple direct metal additive manufacturing processes," in *Proceedings of the Solid Freeform Fabrication Symposium*, Austin, TX, 2013.

[14] J. Beuth and N. Klingbeil, "The role of process variables in laser-based direct metal solid freeform fabrication," *JOM,* journal article vol. 53, no. 9, pp. 36-39, September 01 2001.

[15] A. Vasinonta, J. L. Beuth, and M. Griffith, "Process maps for predicting residual stress and melt pool size in the laser-based fabrication of thin-walled structures," *Journal of Manufacturing Science and Engineering,* vol. 129, no. 1, pp. 101-109, 2007.

[16] I. Maskery *et al.*, "Quantification and characterisation of porosity in selectively laser melted Al–Si10–Mg using X-ray computed tomography," *Materials Characterization,* vol. 111, pp. 193-204, 2016.

[17] H. Gu, H. Gong, D. Pal, K. Rafi, T. Starr, and B. Stucker, "Influences of energy density on porosity and microstructure of selective laser melted 17-4PH stainless steel," in *Proceedings of the Solid Freeform Fabrication Symposium*, Austin, TX, 2013, p. 474.

[18] H. K. Rafi, D. Pal, N. Patil, T. Starr, and B. Stucker, "Microstructure and Mechanical Behavior of 17-4 Precipitation Hardenable Steel Processed by Selective Laser Melting," (in English), *Journal of Materials Engineering and Performance,* vol. 23, no. 12, pp. 4421-4428, 2014/12/01 2014.

[19] H. K. Rafi, T. Starr, and B. Stucker, "A comparison of the tensile, fatigue, and fracture behavior of Ti–6Al–4V and 15-5 PH stainless steel parts made by selective laser melting," (in English), *The International Journal of Advanced Manufacturing Technology,* vol. 69, no. 5-8, pp. 1299-1309, 2013/11/01 2013.

[20] M. Mani, B. M. Lane, M. A. Donmez, S. C. Feng, and S. P. Moylan, "A review on measurement science needs for real-time control of additive manufacturing metal powder bed fusion processes," *International Journal of Production Research,* vol. 55, no. 5, pp. 1400-1418, 2017.

[21] G. Tapia and A. Elwany, "A Review on Process Monitoring and Control in Metal-Based Additive Manufacturing," *Transactions of the ASME, Journal of Manufacturing Science and Engineering,* vol. 136, no. 6, p. 060801, 2014.

[22] M. Mani, B. Lane, A. Donmez, S. Feng, S. Moylan, and R. Fesperman, "NISTIR 8036: Measurement Science Needs for Real-time Control of Additive Manufacturing Powder Bed Fusion Processes," NIST, Gaithersburg, MD2015.

[23] T. G. Spears and S. A. Gold, "In-process sensing in selective laser melting (SLM) additive manufacturing," *Integrating Materials and Manufacturing Innovation,* vol. 5, no. 1, p. 2, 2016.

[24] B. Lane *et al.*, "Thermographic measurements of the commercial laser powder bed fusion process at NIST,"

Rapid prototyping journal, vol. 22, no. 5, pp. 778-787, 2016.

[25] B. Lane, E. Whitenton, and S. Moylan, "Multiple sensor detection of process phenomena in laser powder bed fusion," in *SPIE Commercial+ Scientific Sensing and Imaging*, 2016, pp. 986104-986104-9: International Society for Optics and Photonics.

[26] E. Reutzel and A. Nassar, "A survey of sensing and control for metal-based additive manufacturing," in *Proceedings of the Solid Freeform Fabrication Conference*, 2014.

[27] B. Foster, E. Reutzel, A. Nassar, B. Hall, S. Brown, and C. Dickman, "Optical, layerwise monitoring of powder bed fusion," in *Proceedings of the Solid Freeform Fabrication Symposium*, 2015, pp. 295-307.

[28] A. Nassar, T. Spurgeon, and E. Reutzel, "Sensing defects during directed-energy additive manufacturing of metal parts using optical emissions spectroscopy," in *Proceedings of the Solid Freeform Fabrication Symposium*, Austin, TX, 2014.

[29] A. J. Dunbar, A. R. Nassar, E. W. Reutzel, and J. J. Blecher, "A real-time communication architecture for metal powder bed fusion additive manufacturing," in *Proceedings of the Solid Freeform Fabrication Symposium*, Austin, TX, 2016, pp. 67-80.

[30] B. K. Foster, E. W. Reutzel, A. R. Nassar, C. J. Dickman, and B. T. Hall, "A brief survey of sensing for additive manufacturing," in *SPIE Sensing Technology+ Applications*, 2015, pp. 94890B-94890B-10: International Society for Optics and Photonics.

[31] M. Abdelrahman, E. W. Reutzel, A. R. Nassar, and T. L. Starr, "Flaw detection in powder bed fusion using optical imaging," *Additive Manufacturing,* vol. 15, pp. 1-11, 2017.

[32] P. Boulware, "Final Technical Report to National Institute of Standards and Technology and National Center for Defense Manufacturing and Machining - Measurement Science Innovation Program for Additive Manufacturing: An Evaluation of In-Process Sensing Techniques Through the Use of an Open Architecture Laser Powder Bed Fusion Platform," Edison Welding Institute (EWI), Cincinnati, OHNIST# 70NANB13H192 - 20140097, 2016.

[33] S. Berumen, F. Bechmann, S. Lindner, J.-P. Kruth, and T. Craeghs, "Quality control of laser- and powder bed-based Additive Manufacturing (AM) technologies," *Physics Procedia,* vol. 5, pp. 617-622, 2010.

[34] T. Craeghs, F. Bechmann, S. Berumen, and J.-P. Kruth, "Feedback control of Layerwise Laser Melting using optical sensors," *Physics Procedia,* vol. 5, pp. 505-514, 2010.

[35] T. Craeghs, S. Clijsters, J. P. Kruth, F. Bechmann, and M. C. Ebert, "Detection of Process Failures in Layerwise Laser Melting with Optical Process Monitoring," *Physics Procedia,* vol. 39, pp. 753-759, 2012.

[36] T. Craeghs, S. Clijsters, E. Yasa, F. Bechmann, S. Berumen, and J.-P. Kruth, "Determination of geometrical factors in Layerwise Laser Melting using optical process monitoring," *Optics and Lasers in Engineering,* vol. 49, no. 12, pp. 1440-1446, 2011.

[37] T. Craeghs, S. Clijsters, E. Yasa, and J.-P. Kruth, "Online quality control of selective laser melting," in *Proceedings of the Solid Freeform Fabrication Symposium*, Austin, TX, 2011.

[38] J. z. Jacobsmuhlen, S. Kleszczynski, D. Schneider, and G. Witt, "High resolution imaging for inspection of Laser Beam Melting systems," in *2013 IEEE International Instrumentation and Measurement Technology Conference*, 2013, pp. 707-712: IEEE.

[39] S. Kleszczynski, J. zur Jacobsmühlen, B. Reinarz, J. T. Sehrt, G. Witt, and D. Merhof, "Improving process stability of laser beam melting systems," in *Fraunhofer Direct Digital Manufacturing Conference*, 2014.

[40] S. Kleszczynski, J. Zur Jacobsmühlen, J. Sehrt, and G. Witt, "Error detection in laser beam melting systems by high resolution imaging," in *Proceedings of the Twenty Third Annual International Solid Freeform Fabrication Symposium*, 2012.

[41] A. Wegner and G. Witt, "Process monitoring in laser sintering using thermal imaging," in *SFF Symposium, Austin, Texas, USA*, 2011, pp. 8-10.

[42] D. Hu and R. Kovacevic, "Sensing, modeling and control for laser-based additive manufacturing," *International Journal of Machine Tools and Manufacture,* vol. 43, no. 1, pp. 51-60, 1// 2003.

[43] S. Barua, T. Sparks, and F. Liou, "Development of low-cost imaging system for laser metal deposition processes," *Rapid Prototyping Journal,* vol. 17, no. 3, pp. 203-210, 2011.

[44] H. Krauss, C. Eschey, and M. Zaeh, "Thermography for monitoring the selective laser melting process," in *Proceedings of the Solid Freeform Fabiraction Conference*, Austin, TX, 2012.

[45] H. Rieder, D. Alexander, M. Spies, J. Bamberg, and T. Hess, "Online Monitoring of Additive Manufacturing Processes Using Ultrasound," in *11th European Conference on Non-Destructive Testing (ECNDT 2014)* Prague, Czech Republic, 2014.

[46] H. Krauss, T. Zeugner, and M. F. Zaeh, "Layerwise Monitoring of the Selective Laser Melting Process by

Thermography," *Physics Procedia,* vol. 56, pp. 64-71, 2014.

[47] L. S. Melvin III, S. Das, and S. Beaman Jr, "Video Microscopy of Selective Laser Sintering," in *Proceedings of the Solid Freeform Fabrication Symposium*, 1994, pp. 34-41.

[48] K. Bartkowiak, "Direct laser deposition process within spectrographic analysis in situ," *Physics Procedia,* vol. 5, pp. 623-629, 2010.

[49] Y. Chivel and I. Smurov, "On-line temperature monitoring in selective laser sintering/melting," *Physics Procedia,* vol. 5, pp. 515-521, 2010.

[50] T. Craeghs, S. Clijsters, E. Yasa, and J.-P. Kruth, "Online quality control of selective laser melting," *Solid Freeform Fabrication Proceedings,* pp. 212-226, 2011.

[51] T. Craeghs, F. Bechmann, S. Berumen, and J. P. Kruth, "Feedback control of Layerwise Laser Melting using optical sensors," *Physics Procedia,* vol. 5, pp. 505-514, 2010.

[52] M. Hirsch *et al.*, "Assessing the capability of in-situ nondestructive analysis during layer based additive manufacture," *Additive Manufacturing,* 2016.

[53] R. J. Smith, M. Hirsch, R. Patel, W. Li, A. T. Clare, and S. D. Sharples, "Spatially resolved acoustic spectroscopy for selective laser melting," *Journal of Materials Processing Technology,* vol. 236, pp. 93-102, 2016/10/01/ 2016.

[54] C. Solomon and T. Breckon, *Fundamentals of Digital Image Processing: A practical approach with examples in Matlab*. John Wiley & Sons, 2011.

[55] F. Chung, "Spectral Graph Theory American Mathematical Society," *Providence, RI,* 1997.

[56] S. Jianbo and J. Malik, "Normalized cuts and image segmentation," *IEEE Transactions on Pattern Analysis and Machine Intelligence,* vol. 22, no. 8, pp. 888-905, 2000.

[57] P. K. Rao, O. F. Beyca, Z. Kong, S. T. Bukkapatnam, K. E. Case, and R. Komanduri, "A graph-theoretic approach for quantification of surface morphology variation and its application to chemical mechanical planarization process," *IIE Transactions,* vol. 47, no. 10, pp. 1088-1111, 2015.

[58] M. S. Tootooni *et al.*, "Online non-contact surface finish measurement in machining using graph theory-based image analysis," *Journal of Manufacturing Systems,* vol. 41, pp. 266-276, 2016/10/01/ 2016.

[59] B. Mohar, "The Laplacian spectrum of graphs," *Graph Theory, Combinatorics, and Applications,* vol. 2, pp. 871-898, 1991.

[60] X. Jiang, P. J. Scott, D. J. Whitehouse, and L. Blunt, "Paradigm shifts in surface metrology. Part 2 : The current shift," *Proceedings of the Royal Society A: Mathematical, Physical and Engineering Science,* vol. 463, no. 2085, pp. 2071-2099, 2007.

[61] B. Yao, F. Imani, A. Sakpal, E. W. Reutzel, and H. Yang, "Multifractal Analysis of Image Profiles for the Characterization and Detection of Defects in Additive Manufacturing (In-Press)," *Transactions of the ASME, Journal of Manufacturing Science and Engineering,* 2017.

[62] C. Kan, C. Cheng, and H. Yang, "Heterogeneous recurrence monitoring of dynamic transients in ultraprecision machining processes," *Journal of Manufacturing Systems,* vol. 41, pp. 178-187, 2016.

[63] L. Meisel, M. Johnson, and P. Cote, "Box-counting multifractal analysis," *Physical Review A,* vol. 45, no. 10, p. 6989, 1992.

[64] M. F. Barnsley and S. Demko, "Iterated function systems and the global construction of fractals," vol. 399, pp. 243-275: The Royal Society.

[65] A. Chhabra and R. V. Jensen, "Direct determination of the f (α) singularity spectrum," *Physical Review Letters,* vol. 62, no. 12, p. 1327, 1989.

[66] D. Fabio, A. Reis, and R. Riera, "Lacunarity calculation in the true fractal limit," *Journal of Physics A: Mathematical and General,* vol. 27, no. 6, p. 1827, 1994.

[67] R. E. Plotnick, R. H. Gardner, W. W. Hargrove, K. Prestegaard, and M. Perlmutter, "Lacunarity analysis: a general technique for the analysis of spatial patterns," *Physical review E,* vol. 53, no. 5, p. 5461, 1996.